J. Fluid Mech. (2009), *vol.* 626, *pp.* 449–475. © 2009 Cambridge University Press
doi:10.1017/S0022112009005904 Printed in the United Kingdom

Experimental and numerical investigation of the Richtmyer–Meshkov instability under re-shock conditions

E. LEINOV[1]†, G. MALAMUD[1,2]†, Y. ELBAZ[2], L. A. LEVIN[1,2],
G. BEN-DOR[1], D. SHVARTS[1,2] AND O. SADOT[1,2]‡

[1]Pearlstone Center for Aeronautical Engineering Studies, Department of Mechanical Engineering,
Ben-Gurion University of the Negev, P.O.B. 653, Be'er-Sheva, Israel

[2]Department of Physics, Nuclear Research Center-Negev, P.O.B. 2001, Be'er-Sheva, Israel

(Received 6 October 2008 and in revised form 26 December 2008)

An experimental and numerical systematic study of the growth of the Richtmyer–Meshkov instability-induced mixing following a re-shock is made, where the initial shock moves from the light fluid to the heavy one, over an incident Mach number range of 1.15–1.45. The evolution of the mixing zone following the re-shock is found to be independent of its amplitude at the time of the re-shock and to depend directly on the strength of the re-shock. A linear growth of the mixing zone with time following the passage of the re-shock and before the arrival of the reflected rarefaction wave is found. Moreover, when the mixing zone width is plotted as a function of the distance travelled, the growth slope is found to be independent of the re-shock strength. A comparison of the experimental results with direct numerical simulation calculations reveals that the linear growth rate of the mixing zone is the result of a bubble competition process.

1. Introduction

When an interface first separating two fluids of different densities is impulsively accelerated, small perturbations, initially located on the interface, grow in the form of light bubbles floating into the heavy fluid and heavy spikes penetrating into the light fluid, and eventually a mixing zone (MZ) is formed. The just-described phenomenon is known as the Richtmyer–Meshkov (RM) instability (Richtmyer 1960; Meshkov 1969). RM instability is closely related to the Rayleigh–Taylor (RT) instability (Strutt 1900; Taylor 1950) and is also referred as the impulsive RT instability. The RT instability portrays the growth of small initial perturbation on a discontinuous interface between two incompressible fluids of different densities under a constant acceleration field. In order for the interface to become unstable, in the RT case, the acceleration has to be opposite in its direction to the density gradient (i.e. $\nabla P \cdot \nabla \rho < 0$). However, in the RM instability case, the interface instability is invariant to the direction of the acceleration (i.e. light/heavy or heavy/light). The RM instability is significant in a variety of current scientific fields of interest such as inertial confinement fusion (ICF) and astrophysics (i.e. super-nova) and has gained much attention in the past decades. In ICF experiments, high-energy lasers are used to create an ablative front and

---

† Equally contributed.
‡ E-mail address for correspondence: sorens@bgu.ac.il

compress ∼1 mm diameter hollow spherical capsule containing solid shell deuterium–tritium (DT) and an inner space filled with gaseous DT. The imploding shock moving towards the centre of the spherical shell induces the RM instability on its inner surface due to the large density difference between the solid and gaseous DT, resulting in a rapid growth of initially present random perturbations. This rapid RM instability development induces mixing of the ablative material of the shell with the gaseous DT, reducing its ability to reach the threshold required to ignite and produce energy (Lindl, McCrory & Campball 1992). Furthermore, after the shock wave has converged to the shell centre, it reflects outwards towards the converging DT shell, and re-shocks it once again, enhancing the mixing process. Another example is the well-known phenomena of super-nova core collapse explosion, in which very strong shocks moving outwards from the explosion centre induce impulsive acceleration on the interfaces separating different materials. In fact, the RM instability has been used in numerical modelling for stellar evolution and might explain the lack of stratification of the products of super-nova 1987A (Arnett 2000). Although good understanding of the MZ evolution due to a single shock-wave interaction is now at hand, not much information is available about the development characteristics of the MZ when it is accelerated by multiple shock waves, with random multi-mode initial perturbations. In the present work, we conducted a comprehensive experimental study, in order to find the physical dependencies of the MZ growth in the post re-shock evolution. The experimental results were also reproduced using full three-dimensional direct numerical simulations (DNS), in order to better understand the physical mechanisms which dominate the MZ evolution. Here, the physical stages of the RM development and theoretical approaches are briefly discussed in §§ 1.1–1.3, and then re-shock systems are comprehensively discussed in § 1.4. The experimental setup and the measurement technique are described in § 2 and the numerical simulations are described in § 3. The experimental and numerical results are reported and discussed in § 4 and our conclusions of the research are provided in § 5.

1.1. *The linear stage and the impulsive model*

Following the linear theory of Taylor (1950), Richtmyer (1960) developed an analytical solution for the first-order perturbed equations of small single-mode perturbations, initially placed on a discontinuous interface between two incompressible fluids under impulsive acceleration (e.g. shock wave), when surface tension and viscosity are neglected, where the acceleration term is given by a Dirac delta function times the velocity jump induced on the interface Δu (i.e. $g = -\Delta u \cdot \delta(t)$) to obtain the impulsive solution

$$u_{imp} = \frac{\partial a}{\partial t} = kA\Delta u a_0, \tag{1.1}$$

where a is the amplitude, a_0 is the initial amplitude, $k = 2\pi/\lambda$ is the wavenumber (λ the wavelength) and $A = (\rho_2 - \rho_1)/(\rho_2 + \rho_1)$ is the Atwood number. The impulsive model solution is valid as long as the perturbation amplitude remains much smaller than its wavelength ($a/\lambda \ll 1$).

1.2. *The early nonlinear and asymptotic stage*

Later on, when the ratio of the perturbation's amplitude to its wavelength grows to be $a/\lambda \sim 1$, harmonics of high-order are introduced into the equations (Zhang & Sohn 1996; Zhang & Sohn 1997), and the instability growth becomes nonlinear. In the second order, these nonlinear harmonics develop asymmetries between the bubbles and the spikes, and in the third order, to velocity reduction due to inertial forces. When the Atwood number is large enough, the perturbed interface can be described as bubbles and spikes, where the bubbles are the penetration of the light fluid into the heavy one while the spikes are the penetration of the heavy fluid into the light one. For the late times, Layzer (1955) described the bubble behaviour using a simple potential flow model, based on an approximate description of the flow near the bubble tip for a steady gravitational field. By developing the interface near the tip to second order, when the tip is described by the velocity potential ($\phi(x, y, z) = a(t)\cos(kx)\mathrm{e}^{-kz}$, $\boldsymbol{V} = \nabla\phi$, where ϕ and $\boldsymbol{V}$ are the velocity potential and the velocity vector relative to the fluid velocity respectively) into the Bernoulli equation, the bubble tip acceleration can be derived as a simple drag equation. At very late times (i.e. $t \to \infty$) the bubble velocity reaches an asymptotic behaviour, evolving as λ/t (Layzer 1955; Alon *et al.* 1994).

1.3. *Multi-mode initial condition*

In the case of multi-mode initial perturbations, nonlinear processes of mode coupling (Haan 1989 and Ofer *et al.* 1996) and equivalently bubble competition (Alon *et al.* 1994, 1995) are dominant. In the bubble competition process, large bubbles overtake the volume originally occupied by smaller bubbles. Due to this mechanism, the average wavelength of the multi-mode perturbed interface increases with time and the width of the overall perturbation grows faster than in the case of a single-mode interface. At late time the perturbation becomes self-similar (SS) and grows in a decaying fashion of $\sim t^{\theta}$, where the value of θ is 0.2 for a three-dimensional flow and 0.4 for a two-dimensional flow for the bubble front (Alon *et al.* 1994, 1995) and in the range of 0.2–1.0 for the spike front, depending on the Atwood number (Oron *et al.* 2001). In the SS stage, there is no memory of the initial conditions, i.e. the initial stage of the evolution has no effect on the later stage. Srebro *et al.* (2003) expanded the validity of the buoyancy-drag approach to all instability stages and modelled the growth of the mixing fronts for a multi-mode perturbation and for a general acceleration profile.

1.4. *Re-shock systems*

In many applications, the mixing layer experiences more than one shock wave, which enhances the mixing process. It has been shown that a second shock (*re-shock*) increases dramatically the growth of the MZ (Andronov *et al.* 1976; Vetter & Sturtevant 1995). First reported post re-shock MZ growth rate was given by Andronov *et al.* (1976), for a heavy/light gas configuration (air/He) using schlieren diagnostic technique in a 4 cm × 12 cm shock tube with the endwall of the test-section placed at 16.9 cm from the initial position of the contact surface. Andronov *et al.* (1982) reported on measurements of the evolution of the RM instability in rectangular and cylindrical geometries for different gas configurations, including two interfaces: air/He, air/He/air, air/Xe/He and gave a more detailed model for turbulent mixing induced by the RM instability. Nikiforov, Andronov & Razin (1995) used the experimental results of Andronov *et al.* (1982) and Zaitsev *et al.* (1985) for comparison with their numerical calculations for different endwall distances; the endwall was placed at locations ranging from 16.9 to 123.8 cm. Brouillette & Sturtevant (1989) reported on the growth induced by multiple shock waves for both heavy/light (air/He) and light/heavy (air/SF_6) gas configurations and for two kinds of interfaces, continuous and discontinuous, using schlieren method visualization. They measured much smaller values of the width of the MZ than Andronov *et al.* (1982) and explained the discrepancies by the presence of a wall-jet in the experiments. Thus, they distinguished between MZ width and a wall-jet width. They proposed to model the evolution of an interface accelerated by multiple shock waves by applying the impulsive solution (1.1) to each shock interaction, thus the growth of the total width of a single-mode interface following N impulsive accelerations, as long as the perturbation remains in the linear regime, i.e. $ka \ll 1$, is obtained as

$$\left(\frac{\partial h}{\partial t}\right)_N = \sum_{i=0}^{N-1} \left(\frac{\partial h}{\partial t}\right)_i = 2k \sum_{i=0}^{N-1} (\Delta u_i A_i^+ a_i^+), \tag{1.2}$$

where $(\partial h/\partial t)_i$ is the impulsive growth rate induced by the ith wave, the first wave interaction corresponding to $i = 0$, k is the initial perturbation wavenumber, Δu_i is the change in the velocity of the interface due to the ith wave, A_i^+ and a_i^+ are the Atwood number and amplitude, respectively, after the passage of the ith wave and the factor 2 accounts for the width (twice the amplitude a). Further investigation by Brouillette & Sturtevant (1993) was undertaken with lower Mach numbers than their earlier investigation, with thin (discontinuous) and thick (continuous) interfaces and both light/heavy (air/SF_6) and heavy/light (SF_6/air) gas configurations. The interface growth increased noticeably following the passage of the re-shock. In both investigations the authors compared their experimental results with a model derived by Mikaelian (1989) for turbulent mixing that takes place after the passage of a single shock. The comparison was made for both MZ growth rates following the incident shock wave and following the re-shock. Mikaelian (1989) applied the Canuto & Goldman (1985) analytical model to turbulence generated by the class of instabilities which have a power-law growth rate. Mikaelian (1989) developed a simple model for turbulence generated by RM instability based on the rocket-rig experimental results of Read (1984) and Youngs (1984) for the growth of the RT unstable mixing layer. Assuming no dependence on the initial conditions and neglecting molecular dissipation effects, Mikaelian (1989) differentiated the result for the RT case, replaced the acceleration due to the gravity with an impulsive acceleration and integrated to obtain

$$\frac{\partial h}{\partial t} = 0.28 \Delta u_1 A_1^+, \tag{1.3}$$

where Δu_1 is the change in the interface velocity resulting from the passage of the re-shock, A_1^+ is the post re-shock Atwood number, h is the overall width of the MZ and the empirical coefficient 0.28 is based on the MZ growth rate obtained from the RT experiments of Read (1984) and Youngs (1984). Later studies by Dimonte & Schneider (2000) and Oron *et al.* (2001) revealed that there is an asymmetry between the fronts of the bubbles and the spikes of the MZ. This asymmetry was found to increase with the Atwood number. Following Dimonte & Schneider (2000) and Oron *et al.* (2001), the growth coefficient in (1.3) is in the range of 0.28–0.39.

Vetter & Sturtevant (1995) studied experimentally the evolution of the RM instability of a light/heavy (air/SF_6) gas configuration in a 17 inch diameter shock tube with a flat membrane initially separating the gases. Wire meshes were used in order to capture the membrane fragments and prevent them from being introduced into the MZ. Several configurations of wire mesh positions relative to the membrane were used and yielded varied MZ growth rates. They found that the flat membrane used to form the initial random-mode perturbations on the contact surface separating the two gases had a non-negligible effect on the MZ growth prior to the interaction with the re-shock, while after the interaction with the re-shock, the MZ was independent of the membrane. They changed the length of the test-section to assure that the interaction of the re-shock with the interface would be in the field of view for different incident Mach number experiments. After the passage of the re-shock through the contact surface, a linear growth was observed and compared with the formulation of Mikaelian (1989), where the error range of the growth rate was found to be within 23 %. Houas & Chemouni (1996) reported on RM instability experiments using different gas configurations (CO_2/Ar, CO_2/He, air/CO_2, air/Ar and air/He) with an initially plane discontinuous interface in two Mach number regimes (2.0–2.4 and 3.7–4.2). Using an air/air experiment they deduced that the membrane does not influence the growth rate measurement of the MZ, but does influence the width measurement of the MZ. Erez *et al.* (2000) studied the effect of the membrane thickness on the evolution of the RM instability in flat (random-mode) and large-amplitude single-mode configurations. They found that the membrane had a significant effect on the MZ during the initial stages of its growth, while in the late time the effect was found to be small, and that post re-shock growth is independent of the membrane. Sadot *et al.* (2000) reported on experimental and numerical investigations of the single-mode nonlinear evolution of the RM instability, following the predictions of Alon *et al.* (1995), suggesting that both RT and RM instabilities are governed by three physical elements: single bubble evolution, single spike evolution and the interaction between neighbouring bubbles. The interface evolution was studied before and after the arrival of the re-shock in a single mode, light/heavy (air/SF_6) configuration. A bubble competition mechanism was demonstrated both before and after the passage of the re-shock. Charakhch'yan (2001) assumed that the re-shock is much weaker than the incident shock wave, and that the re-shock arrives at the single-mode interface during the nonlinear phase, when the amplitude is of the order of magnitude of the wavelength, i.e. $\eta(t) \sim \lambda$. As a result, the change in Atwood number caused by the re-shock could be neglected and the growth rate is given as

$$\frac{\partial h}{\partial t} = 2u_{imp} - 2.5\Delta u_1 A^+, \tag{1.4}$$

where A^+ is the Atwood number following the passage of the initial shock wave, the empirical coefficient 2.5 is based on two-dimensional simulations, u_{imp} is the Richtmyer velocity and Δu_1 is the velocity jump due to the re-shock. The post re-shock descriptions of Brouillette & Sturtevant (1989), Mikaelian (1989) and Charakhch'yan (2001), all reproduced the linear growth rate. Schilling, Latini & Don (2007) performed a numerical analysis of the re-shocked RM instability in a single-mode case and reported calculated post re-shock linear growth rates of 14.44, 11.95 and 14.92 m s^{-1} for the Brouillette & Sturtevant (1989) Mikaelian (1989) and Charakhch'yan (2001) predictions, respectively. A model which is based upon physical characteristics is the Srebro *et al.* (2003) model, which describe the evolution of a multi-mode spectrum of perturbations using a single characteristic wavelength. In the model, self-similar behaviour is assumed together with drag and buoyancy forces. Under these assumptions, bubble and spike fronts can be described for different acceleration profiles, including the re-shock condition, which is the main focus of the present investigation. For further details, see Srebro *et al.* (2003). In all of the above-mentioned experimental studies of the RM instability with re-shock, measurements of the width of the MZ have only been reported in a narrow time period of the evolution of the instability following the re-shock with no systematic analysis of the parameters influencing the evolution of the MZ following the re-shock. In order to better understand the evolution of the instability following the re-shock it is essential to classify its evolution stage and to determine which parameters are dominant in each stage. In this study, two different parameters were controlled and the growth rates of the perturbation were measured. The dependence of the growth rate of the MZ following re-shock on its initial width and on the re-shock strength was investigated. The main purpose of this study is to better understand the physics governing the evolution of the RM instability following re-shock experimentally by systematic control of the initial conditions, while minimizing the uncertainties in the experiments.

2. Experiments

2.1. *Experimental setup*

The experimental investigation of the evolution of the RM instability was conducted in a shock tube facility at the Ben-Gurion University. The shock tube is horizontal, 5.5 m long, has an internal cross-section of 8 cm × 8 cm and shock waves of low to moderate Mach numbers ($M_S \sim 1$–3) are generated in it. A shock wave is launched following the pressurization of the driver section of the shock tube and a predetermined rupture of a Mylar diaphragm, initially separating the driven section from the driver section of the shock tube, using a striking pin. The shock wave interacts with a nitrocellulose diaphragm, which initially separates air from sulfurhexafluoride (SF_6), in the test-section of the shock tube. This head-on collision results in the evolution of the RM instability and subsequent turbulent mixing. This experimental investigation concentrated on air/SF_6 combination that yields a constant Atwood number of 0.67. Pressure histories of the flow in the shock tube were obtained using at least three piezoelectric pressure transducers. Transparent windows were installed in the test-section of the shock tube in order to enable flow visualization. The evolution of the instability was documented by a set of schlieren photographs obtained for each experiment, using a pulsed frequency-doubled Nd^{3+}:YAG laser (532 nm) as the light source and a shutter-less high-speed rotating drum camera. The laser produces 240 ns long pulses with a repetition rate up to 50 kHz and energy of approximately 2.4 mJ per-pulse. The photographs were captured on a high ASA, 35 mm photography film, which in turn was digitized using a film scanner. The photographs were analysed using computerized image analysis on MATLAB® software. Figure 1 presents a schematic diagram of the experimental apparatus.

The diaphragm initially separating the driver section from the driven section in the shock tube was ruptured at the desired instant by an electrically actuated striking pin mounted on a rod inside the driver section. This procedure ensured less than 1 % variation in the incident shock-wave Mach number. The internal cross-section of the test-section of the shock tube is identical to that of the shock tube and is attached to the shock tube by means of a flange. A thin membrane having randomly distributed small-scale perturbations, which have random wavelengths ranging up to $\langle \lambda \rangle \sim 1$ mm, was placed in the test-section between the two investigated gases in order to separate them. Upon the rupture of this membrane by the shock wave, the mixing process commenced. The length of the test-section was determined by positioning the rigid endwall at a location of 80–235 mm downstream of the membrane. Further details of the experimental apparatus and technique are described thoroughly in Erez *et al.* (2000) and Sadot *et al.* (2000). A set of the schlieren pictures from a typical experiment is presented in figure 2. The incident Mach number is 1.2 in air and the endwall position is $d = 98$ mm from the initial position of the separating membrane. The downstream side of the test-section is evident in the frame. The nitrocellulose membrane is at the left hand of the frame, the endwall of the test-section is at the right hand of the frame and SF_6 initially fills the space in between.

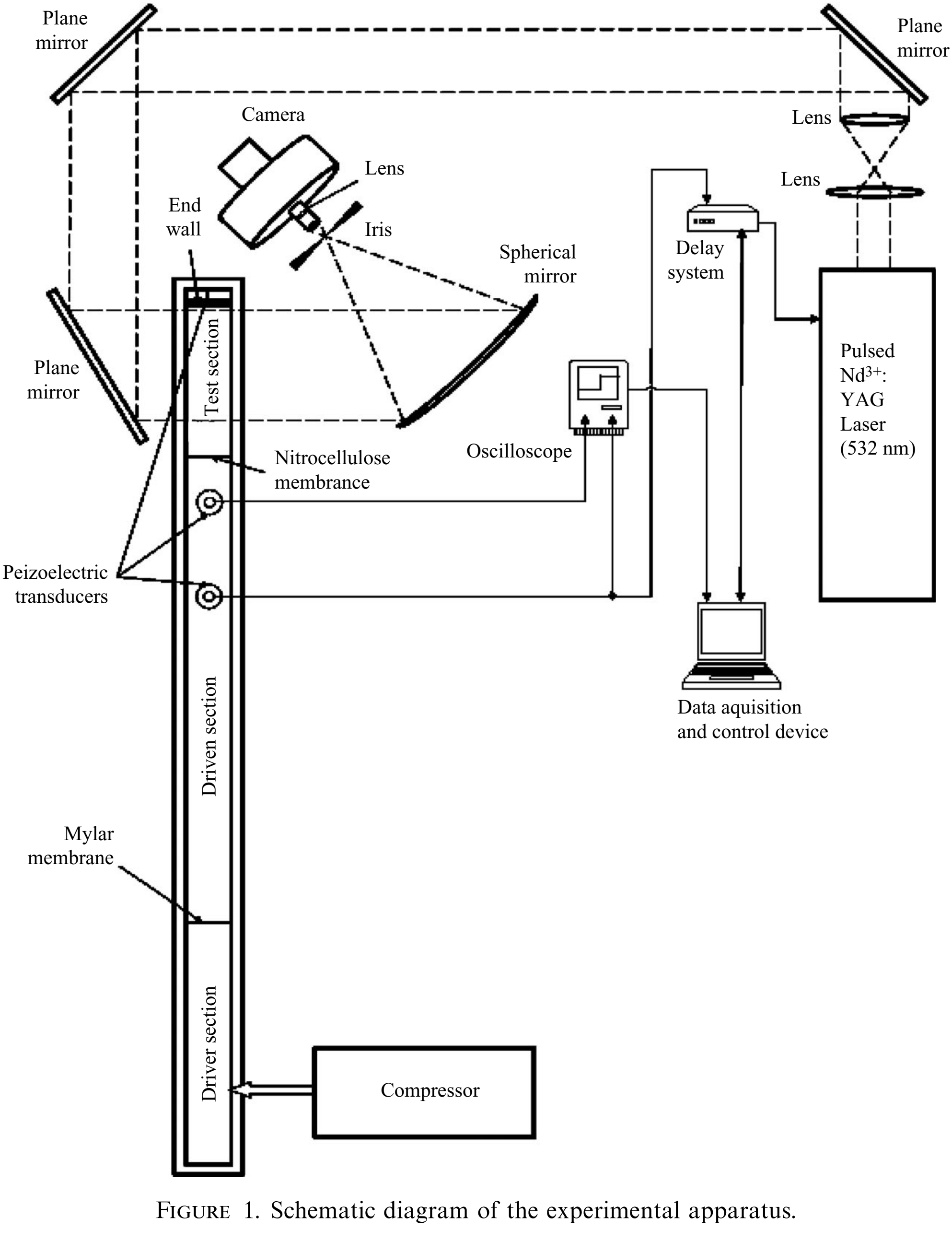

FIGURE 1. Schematic diagram of the experimental apparatus.

The evolution of the RM instability following re-shock in the present study is the result of two successive interactions of two shock waves with the interface, where the first shock wave is the incident shock wave and the second shock wave is the re-shock. Both interactions result in transmitted and reflected waves. Since the main focus of the present investigation is on the evolution of the RM instability following the second interaction, we define the first transmitted shock wave, transmitted into the SF_6 following the first shock-wave interface interaction, as an incident shock wave (ISW) in order to simplify the discussion.

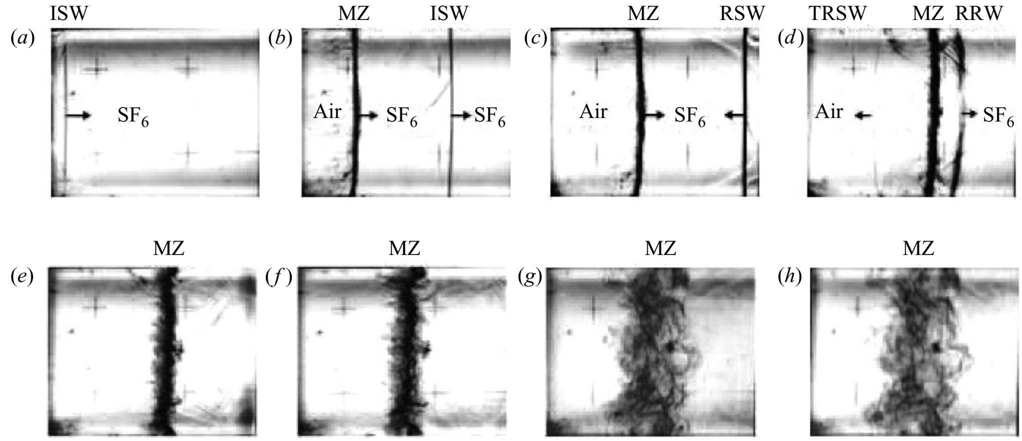

FIGURE 2. Schlieren images from a light to heavy gas configuration (air/SF$_6$) experiment: (*a*) $t = 0.01$ ms, (*b*) $t = 0.34$ ms, (*c*) $t = 0.56$ ms, (*d*) $t = 0.90$ ms, (*e*) $t = 1.07$ ms, (*f*) $t = 1.29$ ms, (*g*) $t = 1.74$ ms and (*h*) $t = 1.96$ ms.

First, the downstream (rightward) moving ISW is evident in figure 2(*a*). The ISW continues moving downstream and the MZ follows it in figure 2(*b*). The MZ separates air on its left side from SF$_6$ on its right side. Following its arrival to the endwall of the test-section, the ISW reflects from it reflected shock wave (RSW) and moves upstream (to the left) towards the evolving MZ, which is moving downstream in figure 2(*c*). Figure 2(*d*) presents the situation just following the interaction of the RSW with the MZ, a shock wave transmitted – reflected shock wave (TRSW), moving upstream, is transmitted to the air and a rarefaction wave (RRW) is reflected towards the SF$_6$ (moving to the right towards the endwall). The dramatic increase in the width of the MZ following the passage of the re-shock is evident clearly in figure 2(*e–h*). Two configurations of the test-section were utilized in the present research. A detailed scheme of the test-sections is given in figure 3. The first configuration (figure 3*a*) consisted of a movable endwall, which enabled controlling the evolution time of the instability prior to the arrival of RSW. The variation of the endwall position was achieved by welding a screwed rod to the centre of a 15 mm thick aluminium plate, which functioned as the endwall. The position of the endwall was fixed by using two bolts, which were adjacent to two plates, adjacent to the frame of the test-section from the inner and outer sides. The second configuration (figure 3*b*) consisted of an elastomeric foam endwall that enabled controlling the strength of RSW while keeping the incident shock-wave strength constant. The elastomeric foam was 105 mm long and had a cross-section that matched the inner cross-section of the test-section, i.e. 80 mm × 80 mm. The elastomeric foam was placed in such a way that one of its faces was adjacent to the aluminium plate that was used as the endwall in the just-described first configuration, and its opposite face, faced upstream. The initial distance of the foam face, facing upstream from the nitrocellulose membrane, was kept at 80 mm. Figure 3(*b*) presents the test-section configuration with the foam endwall. The elastomeric foam was wrapped around and completely covered with a 15 μm thick aluminium foil in order to assure that the elastomeric foam acted as a ‘soft’ wall, which did not disturb the flow in the test-section and the evolution of the instability. In this fashion, shock-wave reflections and small disturbances in the re-shock from the elastomeric foam were avoided. Apart from the aluminium foil, a

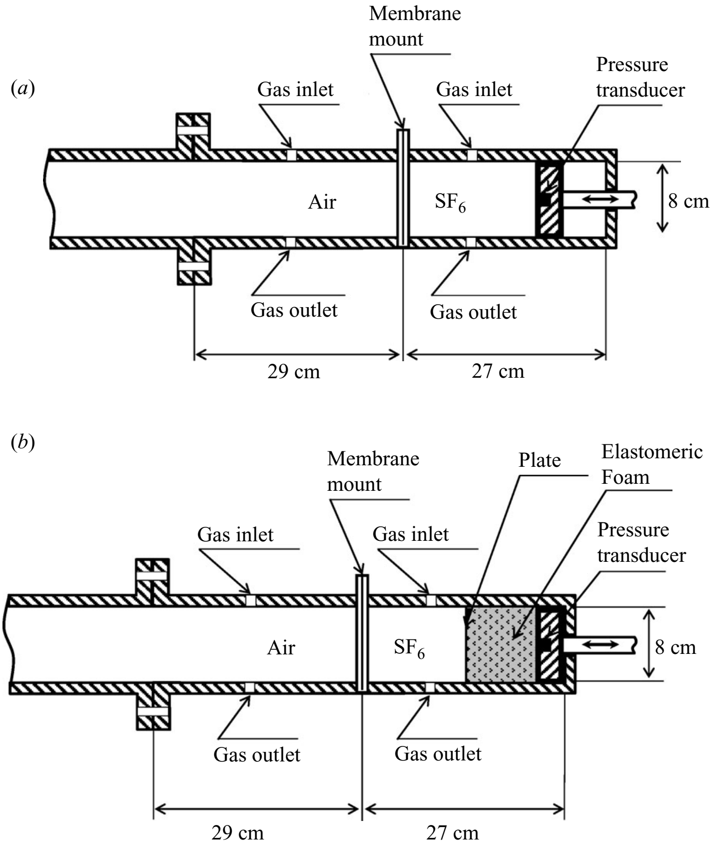

FIGURE 3. Sketch of the test-section: (*a*) the test-section with a movable rigid endwall and (*b*) the test-section with elastomeric foam as an endwall.

plate was bonded to the wrapped face of the foam facing upstream. Three different materials were used as plates: 15 μm thick aluminium foil; 1 mm thick cardboard weighing 2.76 $\pm$ 0.1 g; and a 1 mm thick aluminium plate weighing 16.81 $\pm$ 0.1 g.

2.2. *Measurement technique*

Following the capturing of the schlieren picture on the photographic film, the images were digitized and the position of the visible features such as shock waves, MZ edges and endwall positions were measured digitally. The physical quantities were found from the images using a suitable calibration. From the measured position of the shock wave, the accuracy of the experiment was confirmed, and from the measurements of the MZ edges, the time-dependant MZ width was deduced. Measurements of the MZ boundaries and of the shock waves evident in each photograph were obtained via an in-house MATLAB code. Measurements using this technique ensured an exact determination of the locations of the waves and the boundaries of the MZ using uniform criteria. The code loads a chosen picture file and allows the determination of boundaries and waves in a user-defined region of interest (ROI) from the picture file using an edge detection procedure. This procedure was based on the method of Otsu (1979), which chose the threshold to minimize the intraclass variance of the black and white pixels. The threshold was a normalized intensity value that lay in the range [0, 1]. Two ROIs were defined, one for the MZ and another for the waves.

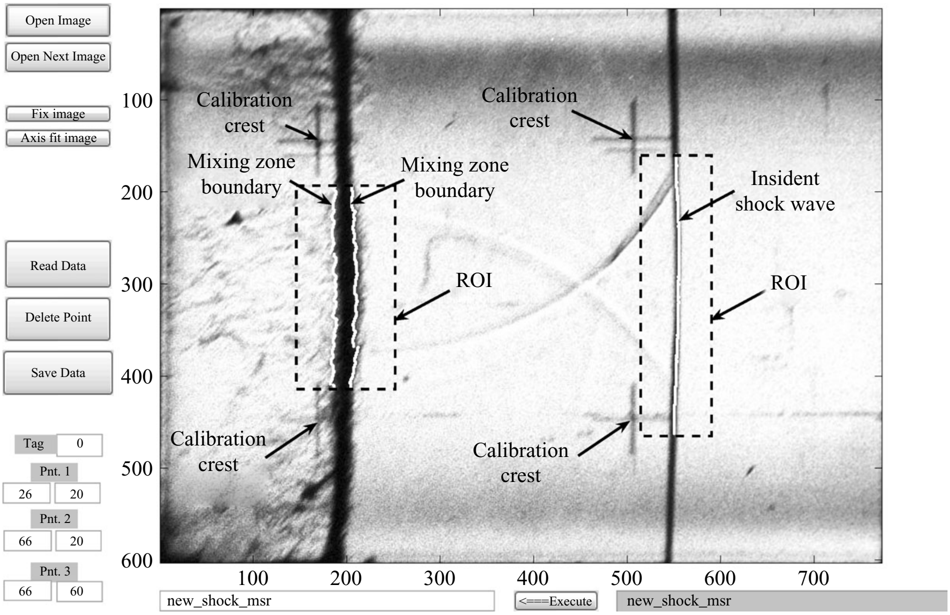

Tag 0

Pnt. 1 26 20

Pnt. 2 66 20

Pnt. 3 66 60

new_shock_msr

new_shock_msr

FIGURE 4. User interface window with an image loaded and processed. Different features found by the code in the user-defined regions of interest (ROI) are coloured white.

The width of each ROI was chosen to be approximately three times larger than the object of interest (i.e. MZ or wave). In order to eliminate wall effects, the height of the ROI was chosen to be in the mid area of the height of the picture, away from the bottom and top walls of the shock tube. The grey scale of each pixel within the ROI was stored, from the digital scan, as a numerical value (between 0 and 255). For each horizontal row of the ROI of the MZ, two pixels were found as the boundaries, one on each side of the MZ. The overall boundary locations of the MZ in a frame were obtained by averaging all the boundary pixels from each side. The overall width of the MZ was obtained by subtracting the averaged boundary locations. The actual physical size of the MZ was then deduced by a comparison with the known length between calibration marks located on the test-section window, which were present on every frame of the experiments and were scanned and digitized in a similar manner. In order to find the locations of the waves, a different algorithm was used. For each horizontal row of pixels in the ROI of the wave, a pixel was found as the maximum grey level. The overall location of the wave in a frame was obtained by averaging all the locations of these pixels. The user interface window from the MATLAB code is presented in figure 4. The selected image occupies most of the window, while on the left there are control buttons which allow the loading of a desired image, defining the physical location of the calibration marks present on every image and selecting the ROIs. Following the ROI selection, the code finds the relevant edges and colours them. In figure 4, the incident shock wave and the left and right boundaries of the MZ are coloured white.

Once a series of images from an experiment has been processed, an x–t and a P-U diagrams could be constructed (figure 5*a,b*), and the time dependence of the overall width of the MZ could be obtained (figure 5*c*). The measurements of the velocities of all the waves are compared with the one-dimensional x–t diagram and the P-U plot corresponding to the conditions of the experiment and the incident shock wave. The

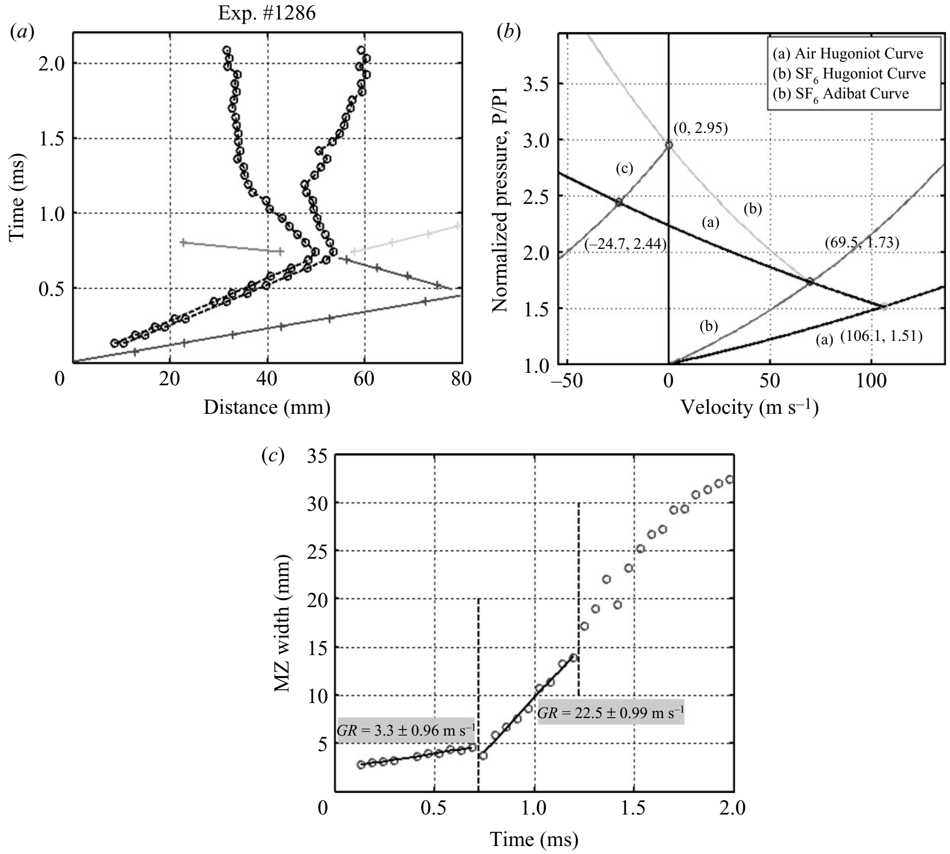

FIGURE 5. Typical experimental processed data: (*a*) an *x–t* diagram, (*b*) a *P-U* plot and (*c*) the MZ width as a function of time.

P-U plot is obtained by means of the Rankine–Hugoniot equation using the incident shock-wave velocity.

3. Numerical simulations

All the simulations presented here were preformed with LEEOR3D (Malamud, Levi-Hevroni & Levy 2003), which is a finite volume ALE (arbitrary Lagrangian Eulerian) hydrodynamic code with interface tracking capability, which solves the Euler equations (viscosity effects are assumed to be negligibly small). The simulations were preformed using a minimum of eight numerical nodes per wavelength at $t = 0$. Hence, a satisfactory numerical description of the growing instability was achieved. The presented DNS were preformed over a 10 mm × 10 mm domain cross-section with 128 × 128 numerical cells. Evidently, this cross-section area allows a fair description of features roughly $\sim$2 mm^2 in size. As will be shown later, the maximal bubble area obtained in the DNS was about 2 mm. Also, very similar results were obtained for a 20 mm × 20 mm DNS. It should be mentioned that numerical convergence was evident by comparing the DNS results for some 256 × 256 numerical-cell simulations. It should also be noted, that the use of DNS in the present study was not for describing small-scale turbulence that occurs inside the MZ, but only in order to obtain a physical understating of the large-scale evolution (i.e. $\langle \lambda \rangle$ 0.2 mm), which dictates the MZ peak to valley (PTV) growth. The one-dimensional initial conditions (incident shock-wave Mach number, initial temperatures and pressure) were obtained from the experimental results, assuming perfect gas equations of state for both air and SF_6, with heat capacities ratios γ of 1.4 and 1.1, respectively. The initial perturbation amplitude for a given spectrum in the DNS was defined by

$$a_0(x, y) = \sum_{k_x, k_y} [a_k \cos(\phi_x)\cos(\phi_y) + b_k \cos(\phi_x)\sin(\phi_y) + c_k \sin(\phi_x)\cos(\phi_y) + d_k \sin(\phi_x)\sin(\phi_y)], \quad (3.1)$$

where $\phi_x = 2\pi k_x x/L$, $\phi_y = 2\pi k_y y/L$ and a_k, b_k, c_k and d_k are random coefficients. Since the initial experimental perturbation spectrum and amplitudes were unknown, the initial DNS perturbation spectrum (defined by k_x and k_y) and amplitude were calibrated using the experimental MZ width of the 80 mm endwall case. Based on the main experimental features of MZ growth (see for example figure 5*c*), four benchmark agreement parameters were defined in order to define the DNS agreement with the experimental results: (i) MZ PTV of $\sim$5 $\pm$1 mm at the re-shock arrival to the MZ; (ii) MZ PTV of $\sim$14 $\pm$1 mm before the arrival of the endwall reflected rarefaction wave to the MZ (0.4 ms following the arrival of the re-shock); (iii) constant growth rate in the time interval following the re-shock passage and the arrival of the endwall reflected refraction wave to the MZ; and (iv) good agreement to the experimental results over the MZ evolution prior to the re-shock arrival to the MZ. After good agreement was achieved for the 80 mm endwall distance, predictions of the numerical model were compared with the experimental results obtained for endwall distances of 172 and 235 mm. Good agreements were obtained. The numerical simulations were then compared also with the experimental results of different re-shock Mach numbers (M_S = 1.15, 1.4 and 1.5) and good agreement was evident again. After the validation of the numerical model was established for all endwall distances, it was tested further by varying the Mach numbers of the incident shock wave, and yet again comparing the DNS results to the experimental data. Again, good agreement was achieved. The profound validity of the numerical model allows us to discuss the physical mechanisms governing the flow field and the evolution of the MZ at post re-shock times.

4. Results & discussion

Experimental results of random-mode initial perturbation evolution following successive impulsive accelerations of a contact surface in a horizontal shock tube facility are reported in this paper. All of the experimental sets reported in this study exhibit successful reproducibility of the evolution of the RM instability under fixed configurations. An experiment was considered as ‘qualified’ once its measurements successfully passed a sequence of matching tests with one-dimensional flow calculations. The comparison with the one-dimensional flow calculations ensured that the velocities of the incident, transmitted and reflected shock waves were within an error smaller than 5 % and the unperturbed one-dimensional contact surface was within the bounds of the measured MZ. Experiment-to-experiment variations were still present due to the turbulent nature of the mixing, but were extremely small. The following sections describe the sets of experiments conducted in order to systematically investigate the evolution of the RM instability following two successive shock-wave accelerations of the contact surface. Two main parameters of the evolution of the

RM instability were the focus of this study: the widths of the MZ at the time of arrival of the re-shock at the MZ and the strength of the re-shock wave. The first main parameter was studied experimentally by varying the endwall position thus varying the re-shock arrival time and allowing the MZ to grow to different widths prior to its interaction with the re-shock. The second main parameter was studied in two experimental sets by varying the incident shock-wave strength at a fixed endwall position and by varying the endwall rigidity at fixed incident shock-wave strength.

4.1. *Growth rate dependence on the MZ width at the time of re-shock*

In order to investigate the evolution of the RM instability following the passage of the shock wave reflected from the test-section endwall, the first parameter that was studied was the width of the MZ at the arrival time of the re-shock. This width was controlled by varying the test-section endwall location and keeping the incident shock-wave Mach number constant. The different endwall distances introduce different time delays over which the MZ can evolve before the arrival of the re-shock. Six different experimental sets at six different endwall locations were selected to test the influence of this parameter. The endwall positions were 80, 98, 131, 172, 199 and 235 mm from the nitrocellulose membrane initially separating the two gases, and the incident shock-wave Mach number was 1.2 in air, which in turn corresponds to a transmitted shock-wave Mach number of 1.3 in SF_6. The MZ measurements for experimental sets of the six endwall distances are presented in figure 6(*a*–*f*). The time scale in figure 6 is shifted so that $t = 0$ is the time when the re-shock arrives at the MZ; the vertical solid black lines represent the time of arrival of the reflected rarefaction wave at the MZ (does not appear in figure 6*e*,*f* since the reflected rarefaction wave arrives after the experimental time period).

Following the passage of the incident shock wave through the membrane, the RM instability starts and quickly grows out of the linear regime into the nonlinear regime. The instability continues to grow with time until the arrival of the re-shock; this time interval corresponds to the shifted time before $t = 0$ in figure 6. The re-shock strikes the MZ and causes it to temporarily contract before it continues to grow. The dramatic increase in the MZ width following the passage of the re-shock appears clearly in all the experimental sets. The MZ appears to grow linearly with time following the passage of the re-shock until the arrival of the rarefaction wave that is also reflected from endwall in the shorter distances and until 0.45 ms in the longest distances. Nevertheless, the MZ width prior to the re-shock arrival was different for each location of the endwall. Figure 7 presents the averaged width for each of the six different endwall positions. The error bar corresponds to the variation among experiments performed in the same set and to the errors in the measurements.

A summary of the MZ widths at the time of the re-shock and the MZ growth rates following it are presented in table 1. Clearly, the growth rates are found to be nearly identical for all the endwall distances. It should be mentioned that the mixing zone growth rates at the longer endwall distances (199 and 235 mm) were calculated for the time period during which a linear growth was observed, i.e. until a shifted time of 0.45 ms. It can clearly be seen from figure 6 that the MZs have reached different widths prior to the arrival of the corresponding re-shocks, while following it they grow at almost the same rate. The growth of the MZ following the passage of the re-shock was treated by applying the least mean squares procedure on the measurements of the MZ widths in order to find the best fit for the data. The procedure was applied to the time period following the passage of the re-shock through the MZ up to the arrival of the rarefaction wave reflected from the endwall and yielded a linear polynomial.

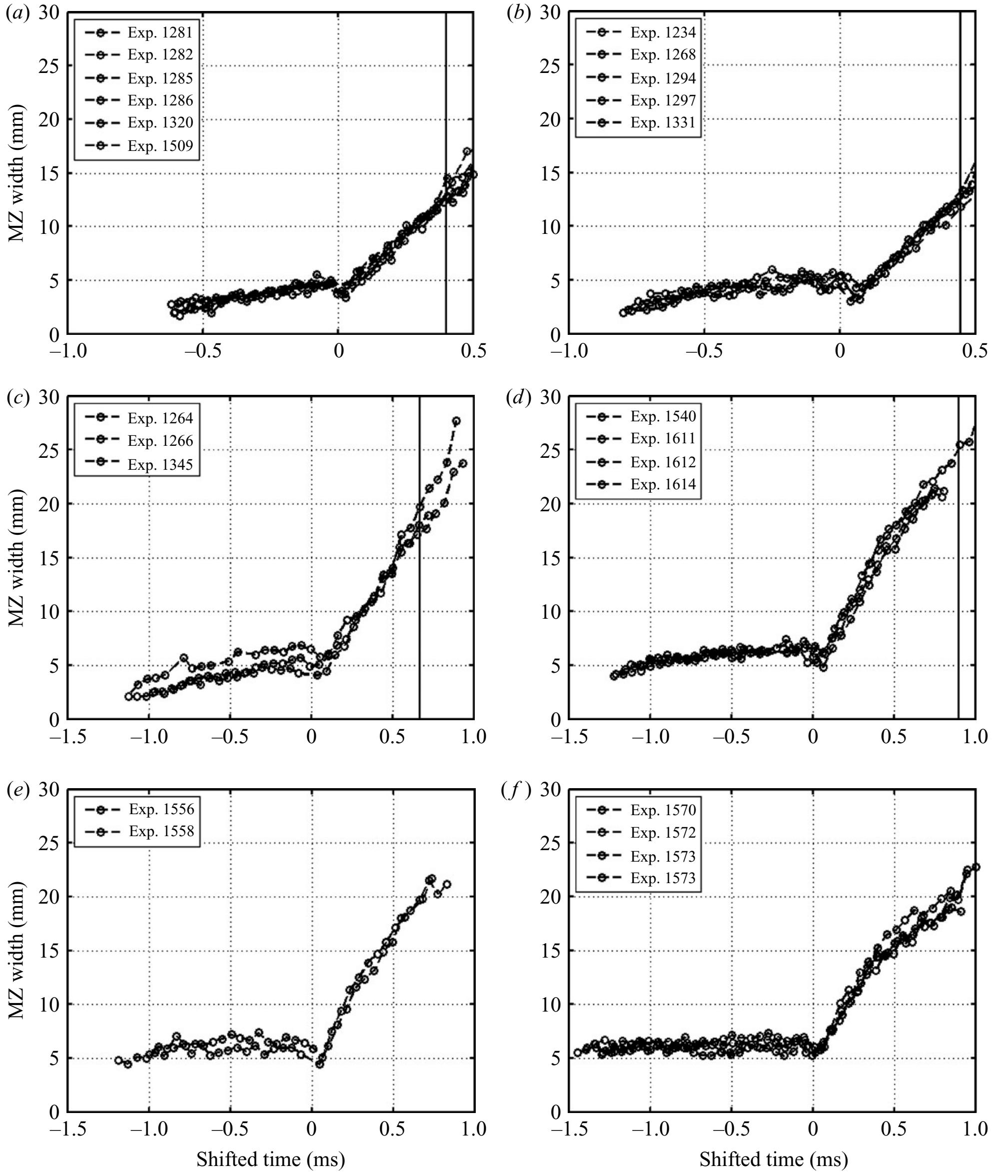

FIGURE 6. Measurements of the width of the MZ as a function of the shifted time for six endwall distances: (*a*) 80 mm, (*b*) 98 mm, (*c*) 131 mm, (*d*) 172 mm, (*e*) 199 mm and (*f*) 235 mm.

The least mean square procedure produced the growth rate of the MZ following the interaction with the re-shock.

As one can see in figure 6(*e*,*f*), as the endwall was placed farther, i.e. at 199 mm and at 235 mm distances, it appears that the unambiguous linear trend observed for the four shorter endwall distances (figure 6*a*–*d*) was broken. Following the passage of the re-shock, the MZ first grew linearly at the same growth rate as in the case of the previous distances, but went into a nonlinear growth at a shifted time larger than about 0.45 ms. The initial growth of the MZ in the experiments with the endwalls located at 199 and 235 mm was similar to that for the first four distances just

Endwall distance (mm)	Width of the MZ at the re-shock arrival (mm)	Growth rate of the MZ following the re-shock (m s^{-1})
80	4.3 ± 0.7	23.1 ± 1.0
98	5.0 ± 0.7	23.0 ± 1.0
131	5.5 ± 0.7	21.8 ± 1.0
172	6.7 ± 0.7	23.0 ± 1.0
199	6.2 ± 0.7	24.3 ± 1.0
235	6.3 ± 0.7	23.8 ± 1.0

TABLE 1. Mixing zone widths at the time of re-shock arrival and growth rates following the re-shock for six locations of the endwall.

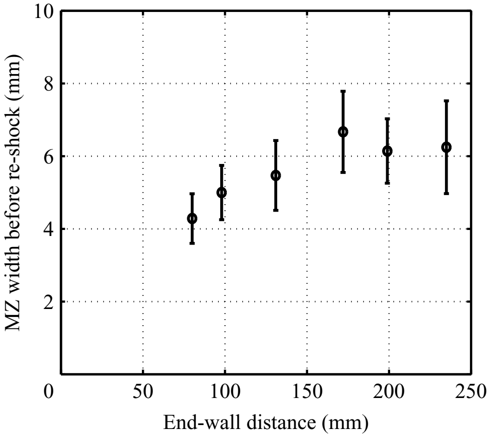

FIGURE 7. Averaged MZ width at the arrival time of the re-shock as a function of the endwall distance.

following the passage of the re-shock as can be seen from table 1, while at later times they diverged. In addition, the MZ growth for the 199 mm endwall distance at late times following the re-shock appears to be larger than for 235 mm, although the difference is within the standard deviation for the MZ measurements. This behaviour can be understood from the inspection of the MZ width prior to the arrival of the re-shock. The initial interface spectrum of the wavelengths was identical in all the experimental sets since the nitrocellulose membrane was fabricated and placed onto its frame and into the test-section in the same manner. For the four shortest endwall distance experimental sets, the MZ is still evolving and its width is increasing up to the point where the re-shock collides with it, while for the longer distances, the MZ appears not to be growing by the time of the arrival of the re-shock. This indicates that, in the latter case, the MZ is in the late nonlinear or asymptotic regime, where it does not grow anymore. Taking into account the experimental parameters for the current experimental sets for calculating the growth rate according to Mikaelian (1989) formulation (1.3), a growth rate of 19.2 ± 1 m s^{-1} was obtained. This result is within 18 % of our experimental results. The post re-shock descriptions of Brouillette & Sturtevant (1989), Mikaelian (1989) and Charakhch'yan (2001), discussed in § 1.4, all reproduced a linear growth rate. As mentioned before, Schilling *et al.* (2007) reported post re-shock linear growth rates of 14.44, 11.95 and 14.92 m s^{-1}

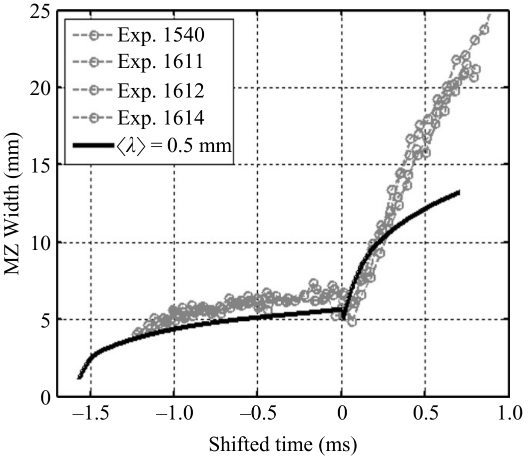

FIGURE 8. Mixing zone growth rate as a function of shifted time, endwall located at 172 mm. Experiments (dashed lines and dots) and multi-mode calculations (solid lines).

for the Brouillette & Sturtevant (1989), Mikaelian (1989) and Charakhch'yan (2001) predictions, respectively. The discrepancy between the growth rates of Brouillette & Sturtevant (1989) and Charakhch'yan (2001) predictions and the growth rates found in the present study are mainly attributed to the fact that the models of Brouillette & Sturtevant (1989) and Charakhch'yan (2001) are valid for the linear regime only and were developed for a single-mode configuration. The discrepancy between the growth rate of Mikaelian (1989) and the growth rates found in the present study is attributed to an empirical coefficient which appears in Mikaelian's description (which arises from RT experiments). This empirical coefficient is in fact a 'free' parameter, which could be adjusted to fit any linear growth rate and does not predict the observed nonlinear growth of the MZ for the longest endwall distance experimental set. The only closed analytic formulation of the evolution of the RM instability in a random-mode situation with re-shock could be found in the model of Srebro *et al.* (2003), which combined the basic buoyancy-drag equation with a simple self-similar wavelength increase relation for the mean bubble wavelength (e.g. $\mathrm{d}\lambda/\mathrm{d}t = u_b/b(A)$, where u_b is the bubble velocity and $b(A)$ is the ratio between the averaged amplitude and the averaged wavelength, dependent on the Atwood number A). Based on this multi-mode model, a calculation was made and compared with the experimental measurement set for the 172 mm endwall distance. The model uses a self-similar assumption, which results in a decay of the MZ growth after the re-shock as can be seen in figure 8. The discrepancy between the model predictions and the experimental results indicates that the evolution of the RM instability following re-shock is not governed solely by a self-similar regime. In fact, in order for the MZ to grow linearly in time, its rate of growth should be constant. The bubble front velocity at late times resulting from the basic buoyancy-drag equation depends (for RM instability) upon a drag term D, which is proportional to the mean wavelength over time, $D \sim \langle\lambda\rangle/t$. Therefore, in order to obtain a bubble front with a constant velocity, the mean wavelength $\langle\lambda\rangle$ should grow linearly in time. This behaviour can exist when an enhanced bubble competition mechanism is involved in the bubble front dynamics, which dictates growth in both the amplitude and the wavelengths, yielding a constant ratio between them, and thus a linear growth of the MZ following the re-shock. This hypothesis was verified using DNS calculations based on the

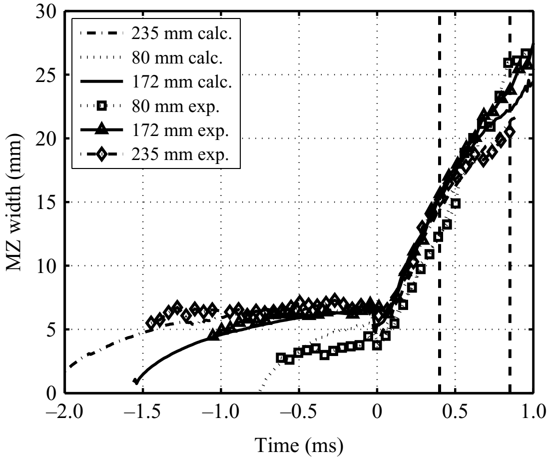

FIGURE 9. Mixing zone width as a function of shifted time, endwall at 80, 172 and 235 mm. Experiments (-□-, -△-, -◇-, respectively) and multi-mode DNS calculations (dotted, solid and dash-dot lines, respectively), Malamud *et al.* (2008). Vertical dashed lines represent the rarefaction wave arrival time in the 80 and 172 mm cases.

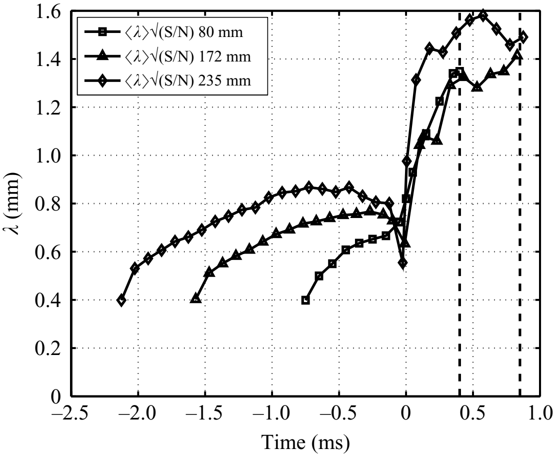

FIGURE 10. Mean wavelengths as a function of shifted time, endwall at 80 mm (-□-), 172 mm (-△-) and 235 mm (-◇-). Vertical dashed lines represent rarefaction wave arrival time in the 80 and 172 mm cases.

LEEOR numerical code (ALE scheme with two-dimensional and three-dimensional capabilities) by Malamud *et al.* (2008). Figures 9–12 present the three-dimensional DNS calculations of Malamud *et al.* (2008).

Very good agreement is obtained between the DNS and the experimental data as evident in figure 9. The agreement is based on the criteria selected for all the different endwall distances: matching of the MZ width at the time of re-shock, matching of the MZ growth prior to the re-shock and matching of the MZ growth rate and width following re-shock. Figure 10 presents the mean wavelengths for three different endwall distances corresponding to the DNS calculations. The mean wavelength is defined by $\sqrt{S/N}$, where S and N are the calculated domain area and the total number of bubbles, respectively. As can be seen, the average wavelength increases

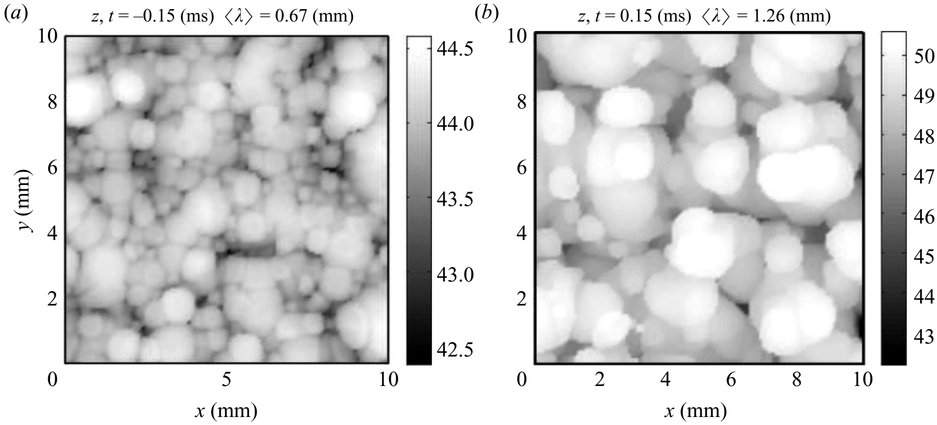

FIGURE 11. DNS bubble front for a 10 mm × 10 mm shock tube cross-section, $\langle \lambda_0 \rangle = 0.4$ mm, endwall at 80 mm. A view from downstream the mixing zone. (*a*) 0.15 ms prior to the interaction with the re-shock and (*b*) 0.15 ms after the interaction with the re-shock.

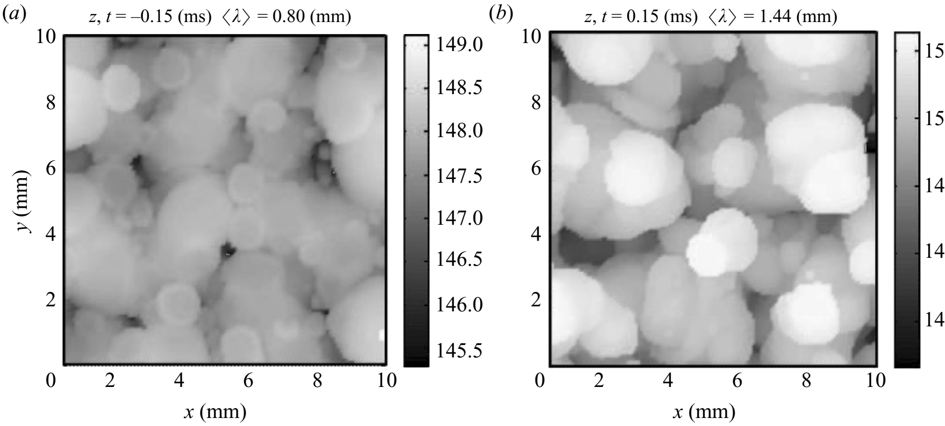

FIGURE 12. DNS bubble front for a 10 mm × 10 mm shock tube cross-section, $\langle \lambda_0 \rangle = 0.4$ mm, endwall at 235 mm. A view from downstream the mixing zone. (*a*) 0.15 ms prior to the interaction with the re-shock and (*b*) 0.15 ms after the interaction with the re-shock.

before the arrival of the re-shock (marked as $t = 0$) for all endwall distances, due to bubble merging process. After re-shock time, the average wavelength increases sharply in all three calculations, growing by more than twice until the arrival of the rarefaction wave (marked with dashed vertical lines, where the left and right vertical dashed lines correspond to experiments performed with the endwall at 80 and 172 mm, respectively). In the shortest distance presented, i.e. endwall located at 80 mm, bubble competition and merging is present after the passage of the re-shock, since the averaged wavelength keeps on increasing, while in the longest distance, i.e. endwall located at 235 mm, the wavelength increases for a very short period of time (about 0.1 ms), followed by almost constant averaged wavelength, which indicates that a single-mode regime dominated the physical problem and is dictating the growth thereafter.

Figures 11 and 12 illustrate the above-discussed physical model by presenting the bubble front amplitudes of the MZ prior and following the re-shock, for two extreme endwall distances: 80 and 235 mm, as was obtained in the DNS. The grey-scale-bars represent the heights in the MZ. The initial mean wavelength which replicates correctly the experimental measurements was found to be $\langle\lambda_0\rangle = 0.4$ mm. The difference between the bubble fronts obtained in the numerical simulation is clearly evident. The typical wavelengths before the re-shock are significantly shorter in the 80 mm endwall case. After the re-shock, this picture remains the same. This difference is due to the longer time period for the bubbles to merge in the 235 mm case with respect to the 80 mm case. This is consistent with the averaged wavelength prior to the re-shock (presented in figure 10), which was ∼8 and ∼6.5 mm in the 235 and 80 mm endwall simulations, respectively. Therefore, it can be seen that the typical merging time in the 80 mm case is shorter than in the 235 mm case. It is also confirmed that a change in the endwall position corresponds to a simple time shift.

4.2. *Growth rate dependence on the re-shock strength*

The dependence of the evolution of the RM instability following the passage of the re-shock on the strength of the re-shock is presented here. The re-shock Mach number was varied in two ways while keeping the endwall distance constant. In the first method, the incident shock-wave Mach number was varied, which caused the re-shock Mach number to vary correspondingly. This method varies not only the re-shock Mach number, but also the extent of mixing in the MZ, which is directly connected to the velocity jump induced by the incident shock wave.

In order to avoid this undesirable occurrence, a second method was introduced to vary the re-shock Mach number, by replacing the solid endwall by elastomeric foam. Three elastomeric foam configurations were used, yielding three different re-shock Mach numbers for the same incident shock-wave Mach number.

4.2.1. *Varied incident shock-wave Mach number*

The incident shock-wave Mach number was varied, causing a corresponding variation in the re-shock Mach number. Three experimental sets with a fixed endwall distance of 80 mm are compared. The width of the MZ at the arrival time of the re-shock was different due to the different velocities induced by the incident shock-waves with different Mach numbers. The MZ measurements from the three experimental sets with different reflected Mach number are presented in figure 13. The time scale in figure 13 is as before, it is shifted so that $t = 0$ is the time when the re-shock arrives at the MZ, the vertical solid lines represent the arrival time of the reflected rarefaction wave at the MZ, and the re-shock Mach number is referred to as M_{ref}.

The measurements were treated in the same fashion as those described in the previous section in order to find the best fit for the data, i.e. by applying the least mean squares procedure to the measurements within the time period following the arrival time of the re-shock at the MZ until the arrival time of the reflected rarefaction wave, yielding the growth rates. Table 2 summarizes the averaged measurement results of the re-shock Mach number, the overall velocity jump experienced by the MZ due to the passage of two successive shock waves (vector sum) and the MZ growth rate for the three experimental sets that are reported in this section.

The three-dimensional DNS calculations with re-shock Mach numbers corresponding to selected experimental values are presented in figure 14. The four values of M_{ref} presented in figure 14 correspond to the calculations. Three of

Experiment	M_{ref}	Overall velocity jump (m s^{-1})	Growth rate (m s^{-1})
Set 1	1.21 ± 0.02	73.0 ± 5.0	13.1 ± 1.5
Set 2	1.30 ± 0.02	96.4 ± 5.0	23.1 ± 1.0
Set 3	1.47 ± 0.03	145.6 ± 10.0	34.6 ± 3.0

TABLE 2. Re-shock Mach number, overall velocity jump and mixing zone growth rates following the re-shock for three experimental sets with a fixed endwall distance of 80 mm.

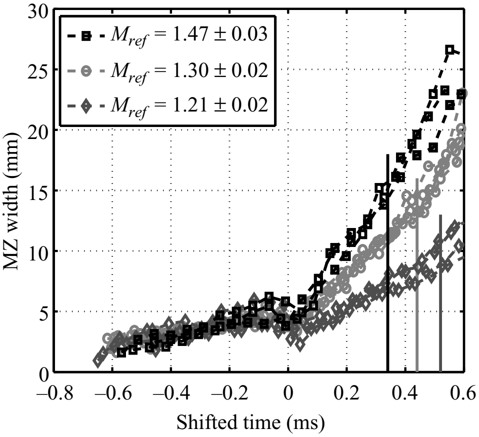

FIGURE 13. Mixing zone width measurements as a function of shifted time for three different incident shock-wave Mach numbers (the endwall is fixed at 80 mm).

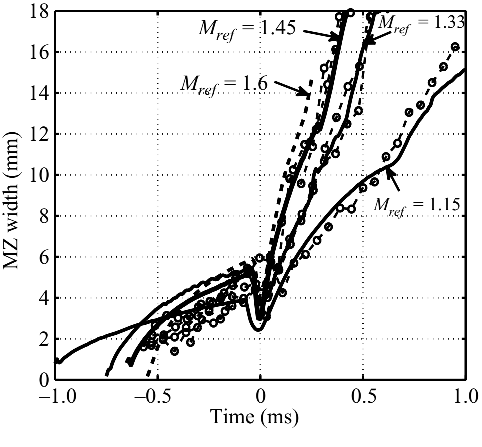

FIGURE 14. Mixing zone width as a function of shifted time for four different re-shock Mach numbers: experiments (dashed lines with circular markers) and multi-mode DNS calculations (solid lines and dashed line).

the calculations are plotted with solid black lines and compared with experiments performed at the re-shock Mach numbers mentioned in the figure, while an additional calculation was made at a higher re-shock Mach number of 1.6. The latter is plotted with dashed black line and the experimental data is plotted with dashed black lines

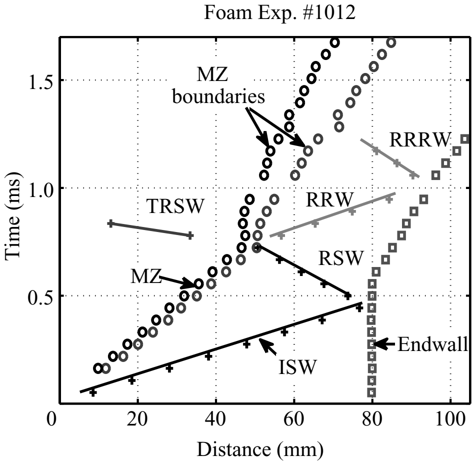

FIGURE 15. An x–t diagram of a typical experiment using an elastomeric foam as an endwall.

with circles. Very good agreement is evident between the three-dimensional DNS calculations and the experimental data. The calculations reproduce the MZ growth trend.

4.2.2. *Varied endwall rigidity*

In the previous subsection the strength of the re-shock was varied by varying the strength of the incident shock wave. This technique also introduced a change in the width of the MZ at the arrival time of the re-shock. This implied that the parameter under consideration, i.e. the re-shock strength, was not the only parameter that was changed. In order to overcome this undesirable situation and assure that the conditions of the MZ remain identical while only the strength of the re-shock is varied, a new experimental technique was introduced. The cross-section of the test-section was identical to that of the previous experiments, but the endwall of the test-section was changed by placing an elastomeric foam adjacent to the rigid endwall of the shock tube (see figure 3*b*). By varying the endwall rigidity, the incident shock wave and the MZ evolution prior to the arrival of the re-shock were identical in the range of the experimental reproducibility in different experiments, while the re-shock strengths varied, hence varying the MZ growth rates. As discussed in § 2.1, three different configurations of elastomeric foams were used and their results were compared with those of the rigid endwall configuration. In all of the configurations with elastomeric foams the plates attached to the front face of the foams (i.e. the face facing upstream) were initially at a distance of 80 mm downstream from the initial position of the membrane. An x–t diagram from a typical experiment with an elastomeric foam as an endwall is shown in figure 15. As a result of the head-on collision of the incident shock wave with the front face of the elastomeric foam, the front face of the elastomeric foam begins to move downstream at a constant velocity following a short period of acceleration. Its position measurements are marked in figure 15 with open squares.

The MZ measurements from the three different configurations of elastomeric foams and from the rigid endwall configuration at 80 mm are plotted in figure 16. It can clearly be seen that as the Mach number of the re-shock increases, the MZ growth rate following its passage also increases.

Endwall feature	Re-shock Mach number (M_{ref})	Overall velocity jump (m s^{-1})	Growth rate (m s^{-1})
Elastomeric foam	1.09 ± 0.03	36.3 ± 6.0	10.5 ± 0.8
Elastomeric foam & cardboard	1.19 ± 0.01	45.4 ± 5.0	14.3 ± 1.0
Elastomeric foam & aluminium plate	1.25 ± 0.02	73.0 ± 6.0	19.7 ± 1.0
Rigid	1.30 ± 0.02	96.4 ± 5.0	23.1 ± 1.0

TABLE 3. Re-shock Mach numbers, overall velocity jumps and the growth rates of the mixing zone following re-shock for four experimental sets with different endwall rigidity. The endwall is at 80 mm.

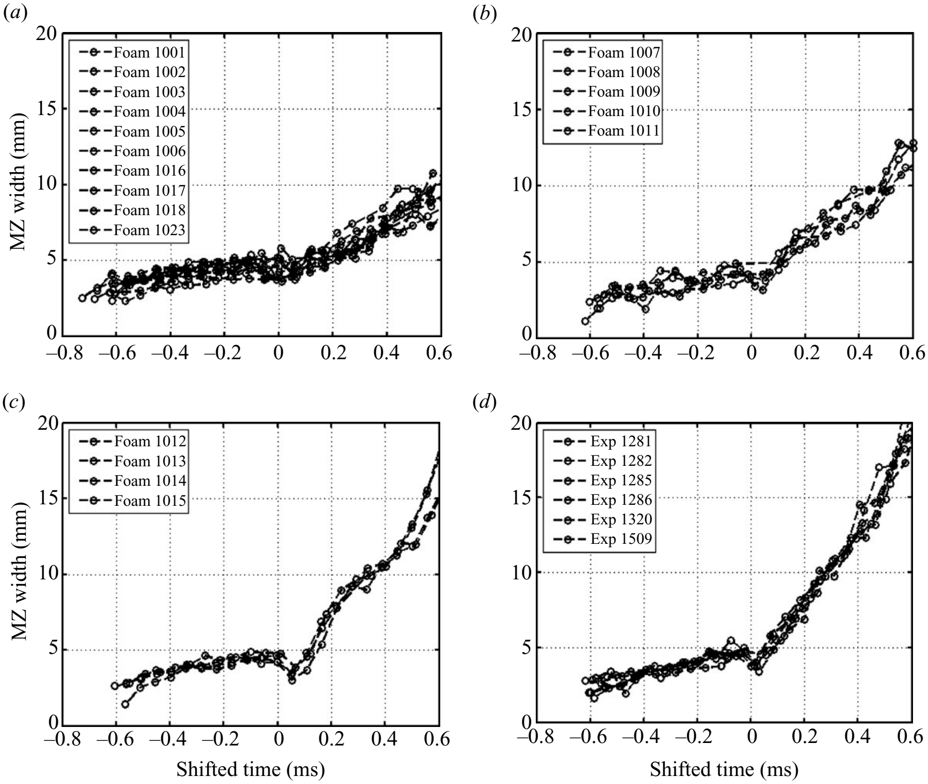

FIGURE 16. Mixing zone width measurements as a function of shifted time for four different endwall rigidities. All the endwalls are at 80 mm: (*a*) elastomeric foam endwall, (*b*) elastomeric foam and cardboard endwall, (*c*) elastomeric foam and aluminium plate endwall and (*d*) rigid endwall.

The measurements were treated in the same fashion as those mentioned in the previous section to find the best fit for the data, i.e. by applying the least mean squares procedure to the measurements within the time period following the arrival time of the re-shock at the MZ until the arrival time of the reflected rarefaction wave, yielding the growth rates. Table 3 summarizes the averaged measurement results of the re-shock Mach number, the overall velocity jump experienced by the MZ due

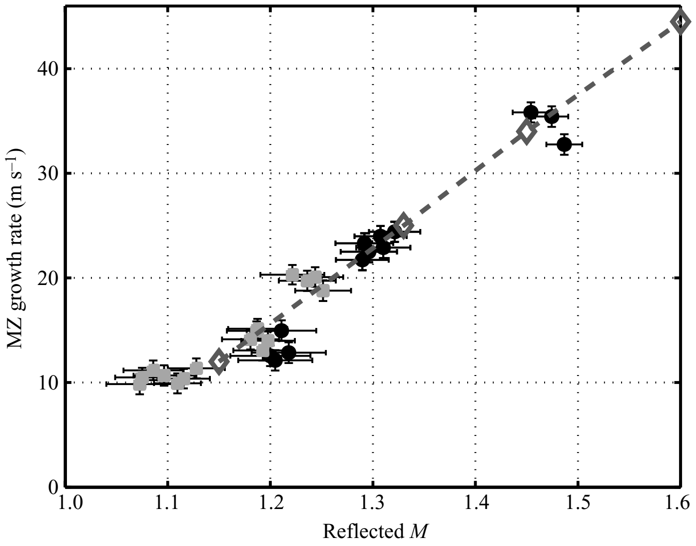

FIGURE 17. Mixing zone growth rate as a function of re-shock Mach number for six different experimental sets. (●) rigid endwall, (grey □) elastomeric foam endwall and (grey ◇) multi-mode DNS calculations. The endwalls are at 80 mm. Grey dashed line: linear trend line intended to guide the eye.

to the passage of two successive shock waves and the MZ growth rate for the four experimental sets reported in this section.

4.2.3. *Summary*

The growth rate dependence on the strength of the re-shock was studied in this section. The re-shock Mach number was varied in two ways while keeping the endwall distance constant. In the first, the incident shock-wave Mach number was varied. This in turn caused the re-shock Mach number to vary correspondingly. The instability growth rate was found to be closely related to the variations in the re-shock Mach number. As the Mach number increased, the growth rate increased. However, in this method not only the re-shock Mach number was varied, but also the extent of mixing in the MZ, which was directly connected with the velocity jump induced by the incident shock wave. In order to avoid this undesirable situation, a second method was introduced to vary the re-shock Mach number by using an elastomeric foam as the endwall of the shock tube. Three elastomeric foam configurations were used, yielding three different re-shock Mach numbers while maintaining the incident shock-wave Mach number. The experimental results for the instability growth rate following the passage of the re-shock were similar to the previous experimental sets. As the Mach number increased, the growth rate increased. The re-shock Mach number in the experiments varied from about 1.1 to about 1.5. A summary of the different growth rate measurements as a function of the re-shock Mach number and the three-dimensional DNS calculation is presented in figure 17.

A strong connection is evident between the re-shock Mach number and the growth rate of the RM instability following the re-shock. The overlap of the measurement results for the rigid endwall with an incident Mach number of 1.2 in SF_6 and for the elastomeric foams with cardboard endwall with an incident Mach number of 1.3 in

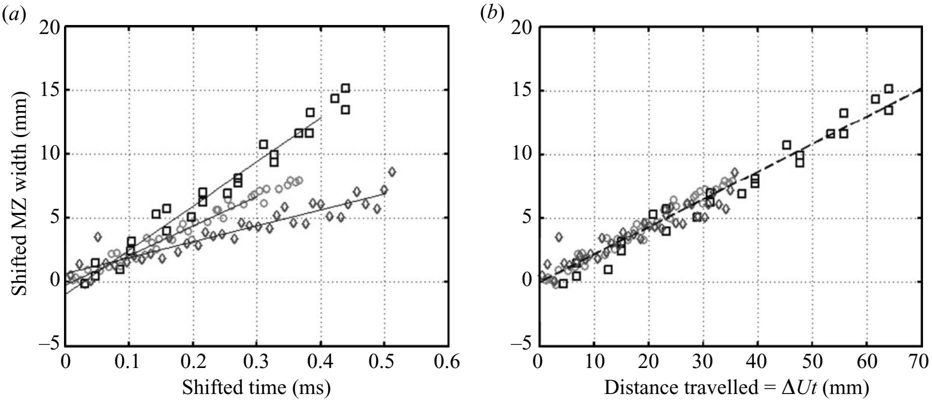

FIGURE 18. Shifted MZ width measurements at different Mach numbers (see figure 13). □ : M_{ref} = 1.47, ◇ : M_{ref} = 1.30 and ○ : M_{ref} = 1.21. (*a*) Shifted MZ width following re-shock ($w - w_{t_{re-shock}}$) and (*b*) shifted MZ width following re-shock ($w - w_{t_{re-shock}}$) versus distance travelled ($\Delta U \cdot t$).

SF_6 strengthens the fact that the growth rate following a re-shock does not depend on the MZ width at the time of the re-shock, but strongly depends on the Mach number. As can be seen from figure 17, good agreement between the calculations and the experimental measurements was found. Since the MZ growth rate following re-shock was found to grow linearly with the re-shock Mach number (figure 17), it was suitable to present the results in distance coordinates rather than shifted time, as can be seen in figure 18. The distance travelled was calculated by $\Delta U \cdot t_{shift}$, where ΔU and t_{shift} are the overall velocity jump induced following the re-shock on the MZ and shifted time, respectively. The MZ width measurements were shifted by the MZ width at the re-shock arrival time ($w - w_{t_{re-shock}}$, where w is the MZ width). Once the abscissa units of shifted time (figure 18*a*) were transformed to distance travelled (figure 18*b*), the MZ width measurements from the three different re-shock Mach number experimental sets collapsed on each other. Thus, the post-re-shock MZ width is found to depend linearly on the distance travelled by the MZ. The dashed line in figure 18(*b*) represents the linear trend line produced by the least mean squares procedure we have performed upon the results. The dimensionless slope of the linear trend line was found to be 0.22 ± 0.01. It should be mentioned that the experiments performed in the current study were conducted with an Atwood number of 0.67. It is anticipated here that the dimensionless slope found above should depend on the Atwood number.

In order to compare our experimental results with the coefficient (0.28) found by Mikaelian (1989) from his formulation for the growth rate (1.3) and the growth coefficient range (0.28–0.39), we found the corresponding dimensionless coefficient values for our experimental sets, using a post re-shock Atwood number of 0.712. Figure 19 presents the dimensionless coefficients for five different experimental sets (black dots), yielding an averaged value of 0.38, and the growth coefficient range (grey area), bounded by a lower limit of 0.28 and an upper limit of 0.39.

It should be mentioned that the coefficients found in Brouillette & Sturtevant (1989) and Charakhch'yan (2001) are not compared on the same plot since unlike the multi-mode configuration of the experiments reported in this study, their coefficients are obtained for a single-mode configuration.

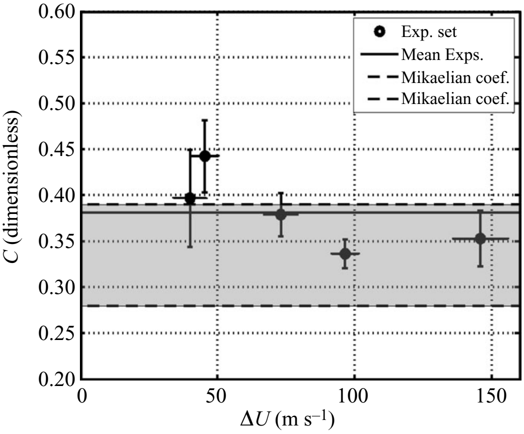

FIGURE 19. MZ growth rate dimensionless coefficients for different experimental sets (dots) and range of growth coefficient (grey area). $C = \mathrm{d}h/\mathrm{d}t \cdot 1/(A\Delta U)$.

5. Conclusions

The interaction of two successive shock waves: the incident and the reflected shock waves, with a random mode perturbed interface, initially separating two gases of different densities, has been studied experimentally. The main focus of this study was to systematically study the growth of the MZ with time following the passage of the re-shock. The dependence of the MZ growth following the passage of the re-shock on two main parameters was investigated: the initial amplitude of the MZ at the arrival time of the re-shock and the re-shock strength. A linear growth of the MZ with time following the passage of the re-shock and before the arrival of the reflected rarefaction wave was found. There was no dependence on the amplitude of the MZ at the arrival time of the re-shock. The re-shock Mach number was found to be a dominant parameter, influencing dramatically the evolution of the MZ following the passage of the re-shock. Furthermore, the MZ width was found to evolve linearly with the distance travelled by the MZ. A comparison of the experimental results with our DNS calculations revealed that the linear growth rate of the MZ is the result of a bubble competition process. The MZ nonlinear growth behaviour prior to the arrival of the reflected rarefaction wave following a linear growth that was evident in the two longest endwall position experimental sets is a result of a single wavelength dominating the physical problem and dictating the decaying growth of the MZ. In addition, the assumption of self-similarity immediately following the re-shock does not reproduce the experimental results and was thus found to be inadequate to model the whole physical picture following a re-shock. The main achievement of this study is the systematic investigation of the RM instability growth following a re-shock over a range of low re-shock Mach numbers: 1.1–1.5, using different techniques and high-quality experiments that have passed different experimental quality tests. The physical depiction of the re-shocked RM instability was portrayed with the support of DNS calculations, and a clear physical understanding of the processes that govern the evolution of the RM instability following re-shock was gained.

The authors would like to acknowledge the useful technical assistance of Mr D. Hirshler. This research was partly supported by Grant No. 2002223 from the United States – Israel Binational Science Foundation (BSF). The financial support of the

Israel Atomic Energy Commission and the Budgeting and Planning Committee of the Council of Higher Education are also acknowledged.

REFERENCES

Alon, U., Hecht, J., Mukamel, D. & Shvarts, D. 1994 Scale invariant mixing rates of hydrodynamically unstable interfaces. *Phys. Rev. Lett.* **72** (4), 2867–2870.

Alon, U., Hecht, J., Ofer, D. & Shvarts, D. 1995 Power laws and similarity of Rayleigh–Taylor and Richtmyer–Meshkov mixing fronts at all density ratios. *Phys. Rev. Lett.* **74** (4), 534–537.

Andronov, V. A., Bakhrakh, S. M., Meahkov, E. E., Mokhov, V. N., Nikiforov, V. V., Pevnitskii, A. V. & Tolshmyakov, A. I. 1976 Turbulent mixing at contact surface accelerated by shock waves. *Sov. Phys. JETP* **44** (2), 424–427.

Andronov, V. A., Bakhrakh, S. M., Meahkov, E. E., Nikiforov, V. V., Pevnitskii, A. V. & Tolshmyakov, A. I. 1982 An experimental investigation and numerical modeling of turbulent mixing in one-dimensional flows. *Sov. Phys. Dokl.* **27** (5), 393–396.

Arnett, D. 2000 The role of mixing in astrophysics. *Astrophys. J. Supp.* **127**, 213–217.

Brouillette, M. & Sturtevant, B. 1989 Richtmyer–Meshkov instability at a continuous interface. In *Current Topics in Shock Waves: 17th International Symposium on Shock Waves and Shock Tubes* (ed. T. W. Kim). AIP Conf. Proceedings, 208, pp. 284–289. AIP.

Brouillette, M. & Sturtevant, B. 1993 Experiments on the Richtmyer–Meshkov instability: small-scale perturbations on a plane interface. *Phys. Fluids* A **5**(4), 916–930.

Canuto, V. M. & Goldman, I. 1985 Analytical model for large scale turbulence. *Phys. Rev. Lett.* **54**, 430–433.

Charakhch'yan, A. A. 2001 Reshocking at the non-linear stage of Richtmyer–Meshkov instability. *Plasma Phys. Control. Fusion* **43**, 1169–1179.

Dimonte, G. & Schneider, M. 2000 Density ratio dependence of Rayleigh–Taylor mixing sustained and impulsive acceleration histories. *Phys. Fluids* **12** (2), 304–321.

Erez, L., Sadot, O., Oron, D., Erez, G., Levin, L. A., Shvarts, D. & Ben-Dor, G. 2000 Study of the membrane effect on turbulent mixing measurements in shock tubes. *Shock Waves* **10**, 241–251.

Haan, S. W. 1989 Onset of nonlinear saturation for Rayleigh–Taylor growth in the presence of a full spectrum of modes. *Phys. Rev.* A **39** (11), 5812–5825.

Houas, L. & Chemouni, I. 1996 Experimental investigation of the Richtmyer–Meshkov instability in shock tube. *Phys. Fluids* **8**, 614–624.

Layzer, D. 1955 On the instability of superposed fluids in a gravitational field. *Astrophys. J.* **122** (1), 1–12.

Lindl, J. D., McCrory, R. L. & Campball, E. M. 1992 Progress toward ignition and burn propagation in inertial confinement fusion. *Phys. Today* **45** (9), 32–50.

Malamud, G., Elbaz, Y., Leinov, E., Sadot, O., Shvarts, D. & Ben-Dor, G. 2008 Bubble dynamics effects in re-shock system. In *11th International Workshop on the Physics of Compressible Turbulent Mixing* (ed. G. Dimonte). IWPCTM Proceedings, to be published.

Malamud, G., Levi-Hevroni, D. & Levy, A. 2003 Two-dimensional model for simulating shock-wave interaction with rigid porous materials. *AIAA J.* **41** (4), 663–673.

Meshkov, E. E. 1969 Instability of the interface of two gases accelerated by a shock wave. *Sov. Fluid Dyn.* **4**, 101–108.

Mikaelian, K. O. 1989 Turbulent mixing generated by Rayliegh–Taylor and Richtmyer–Meshkov instabilities. *Phys.* D **36**, 343–357.

Nikiforov, V. V., Andronov, V. A. & Razin, A. N. 1995 Development of a turbulent mixing zone driven by a shock wave. *Sov. Phys. Dokl.* **40** (7), 333–335.

Ofer, D., Alon, U., Shvarts, D., McCrory, R. L. & Verdon, C. P. 1996 Modal model for the nonlinear multimode Rayleigh–Taylor instability. *Phys. Plasmas* **3**, 3073–3090.

Oron, D., Arazi, L., Kartoon, D., Rikanati, A., Alon U. & Shvarts, D. 2001 Dimensionality dependence of the Rayleigh–Taylor and Richtmyer–Meshkov instability late-time scaling laws. *Phys. Plasmas* **8** (6), 2883–2889.

Otsu, N. 1979 A Threshold election method from gray-level histograms. *IEEE Trans. Syst. Man Cybernet.* **9** (1), 62–66.

READ, K. I. 1984 Experimental investigation of turbulent mixing by Rayleigh–Taylor instability. *Phys.* D **12**, 45–58.

RICHTMYER, R. D. 1960 Taylor instability in shock acceleration of compressible fluids. *Commun. Pure Appl. Math.* **13**, 297–319.

SADOT, O., EREZ, L., ORON, D., EREZ, G., BEN-DOR, G., ALON, U, LEVIN, L. A. & SHVARTS, D. 2000 Studies on the nonlinear evolution of the Richtmyer–Meshkov instability. *Astrophys. J. Supp.* **127**, 469–473.

SCHILLING, O., LATINI, M. & DON, W. S. 2007 Physics of reshock and mixing in single-mode Richtmyer-Meshkov instability. *Phys. Rev.* E **76**, 026319.

SREBRO, Y., ELBAZ, Y., SADOT, O., ARAZI, L. & SHVARTS, D. 2003 A general buoyancy-drag model for the evolution of the Rayleigh–Taylor and Richtmyer–Meshkov instabilities. *Laser Particle Beams* **21**, 347–353.

STRUTT, J. W. (LORD RAYLEIGH) 1900 Investigation of the character of the equilibrium of an incompressible heavy fluid of variable density. In *Scientific Papers*, vol. 2, pp. 200–207. Dover.

TAYLOR, G. I. 1950 The instability of liquid surfaces when accelerated in a direction perpendicular to their planes. *Proc. R. Soc.* A **201**, 192–196.

VETTER, M. & STURTEVANT, B. 1995 Experiments on the Richtmyer–Meshkov instability of an air/SF_6 interface. *Shock Waves* **4** (5), 247–252.

YOUNGS, D. L. 1984 Numerical simulation of turbulent mixing by Rayleigh–Taylor instability. *Phys.* D **12**, 32–44.

ZAITSEV, S. G., LAZAREVA, E. V., CHERNUKA, V. V. & BELYAEV, V. M. 1985 Intensification of mixing at the interface between media of different densities upon the passage of a shock wave through it. *Sov. Phys. Dokl.* **30**, 579–581.

ZHANG, Q. & SOHN, S. 1996 An analytical nonlinear theory of Richtmyer–Meshkov instability driven by cylindrical shocks. *Phys. Lett* A **212**, 149–155.

ZHANG, Q. & SOHN, S. 1997 Nonlinear theory of unstable fluid mixing driven by shock wave. *Phys. Fluids* **9** (4), 1106–1124.